



# Impact of the tilted cloud vertical structure on a northward-progress episode of the East Asian summer monsoonal precipitation belt

Yunying Li<sup>1,2</sup> · Guorong Sun<sup>3</sup> · Zhiwei Zhang<sup>1,4</sup> · Chao Zhang<sup>1,2</sup> · Laurant Li<sup>5</sup>

Received: 17 December 2023 / Accepted: 26 March 2024  
© The Author(s) 2024

## Abstract

Impact of cloud vertical structure (CVS) on a northward-progressing rainfall episode of the East Asian summer monsoon (EASM) is explored using the Weather Research and Forecasting model, in which CloudSat observation-based vertical structure of cloud liquid water content (LWC) can be imposed. Composite LWC anomaly from CloudSat data shows a northward tilted structure from the upper to the lower troposphere. Compared to the control simulation (without modification of LWC), the one with LWC imposed, but without tilted structure, doesn't show significant changes. When LWC is introduced and northward tilted, the geopotential height (HGT) decreases in the north of the convective center, which increases the meridional wind and provides favorable conditions for the northward shift of the precipitation belt. When LWC is southward tilted, HGT decreases in the middle and lower troposphere in the south of the convective center and increases in the north, which slows down the northward shift of the precipitation belt. Adding cloud water leads to increase in humidity and decrease in temperature, causing significant increase in stratiform clouds and related precipitation. In the configuration of northward tilted LWC, low-temperature and high-humidity area is located on the north side of the convective center, favorable for the occurrence and northward shift of the precipitation belt. Deep convection is weakened with convective precipitation reduced, while shallow convection enhances the latent heat release in the lower troposphere. Therefore, more water vapor and energy are transported from boundary layer to free atmosphere, promoting the northward shift of the precipitation belt.

## 1 Introduction

Cloud vertical structure (CVS), comprising the vertical distribution of cloudiness and cloud microphysical parameters in the atmosphere, can result from complex thermodynamic and dynamic processes as well as microphysical processes within clouds (Wang and Rossow 1998; Weare 2000; Wang et al. 2000). The formation and development of clouds cause variation of atmospheric diabatic processes, thereby modify the vertical distribution of atmospheric heating and cooling rates (McFarlane et al. 2008; Turner et al. 2018), which directly affects the atmospheric circulation (Cao and Zhang 2017). Clouds at different altitudes have different radiation effects, their location and vertical overlapping affect the radiation balance of the atmosphere (Hong et al. 2016; Hill et al. 2018). The CVS also affects the microphysics in clouds, influencing the occurrence and intensity

✉ Yunying Li  
liyuning@nudt.edu.cn

<sup>1</sup> College of Meteorology and Oceanography, National University of Defense Technology, Changsha 410073, China

<sup>2</sup> High Impact Weather Key Laboratory of CMA, Changsha, China

<sup>3</sup> Unit No. 92859 of Chinese People's Liberation Army, Tianjin 300000, China

<sup>4</sup> Unit No. 92192 of Chinese People's Liberation Army, Ningbo 315000, China

<sup>5</sup> Laboratoire de Météorologie Dynamique, CNRS, Sorbonne Université, Paris 75005, France

of precipitation (Jakob and Klein 1999; Yan et al. 2018). Despite important progresses of research on the issue since a few years, CVS still remains a main source of uncertainty for climate studies at global scale (Jiang et al. 2012; Cesana and Chepfer 2012; Klein et al. 2013; Zelinka et al. 2013), or at regional scale in East Asia (Zhang and Li 2013; Kusunoki and Arakawa 2015).

CVS is strongly connected to the East Asian summer monsoon (EASM). Impact of the EASM activities on the associated cloud system has been widely studied (Luo et al. 2011; Yuan et al. 2011; Zhang et al. 2020; Zhang and Li 2020), but how cloud properties (macrophysics and microphysics) can exert impact on EASM precipitation has not received sufficient attention. It is to be noted that the CVS is northward tilted from the upper to the lower atmosphere during the northward shift of the EASM activity (Sun et al. 2019a). What role does this tilted CVS play in the northward shift of the EASM progress, and how does it affect the EASM precipitation? This is the main question to address in the present work, through numerical modelling. Actually, a CVS anomaly, as deduced from observation, is constructed and imposed to the Weather Research and Forecasting (WRF) model. It constitutes a typical case to explore the impact of the tilted CVS on the EASM precipitation belt. We also pay attention to any physical mechanisms behind the feedback.

The remainder of this paper is organized as follows. Section 2 provides a description of the data, experimental design and evaluation of WRF simulation. Section 3 presents the impact of the tilted CVS on the EASM precipitation belt, and relevant explanations are explored in Section 4. Finally, Section 5 concludes this paper.

## 2 Data and methods

### 2.1 Data

The CloudSat 2B-cloud water content (CWC)-RVOD product is used to reconstruct the CVS. CloudSat is a Sun-synchronous polar-orbiting satellite, designed to detect clouds in the atmospheric column with a 1.1 km (along-track) by 1.3 km (across-track) footprint. There are 125 bins in each vertical profile, and the thickness of bin is about 240 m (Stephens et al. 2018). The 2B-CWC-RVOD product includes retrieved information of cloud ice water content (IWC) and cloud liquid water content (LWC), discriminated by local air temperature: liquid when temperature larger than 0 °C, ice when temperature smaller than -20 °C, and a linear mixture of liquid and ice when temperature ranges from -20 °C to 0 °C (Austin et al. 2009). The 2B-GEOPROF product also provides a confidence value for each bin. When

it is greater than 30, clouds are correctly detected, and the associated uncertainty is less than 2% (Li et al. 2018). Bins near the ground are inevitably contaminated by the surface, and large uncertainties are included in these bins (Li and Zhang 2017). Therefore, bin samples under an altitude of 0.5 km and confidence values of less than 30 are not used in this study.

Merged daily precipitation data released by the National Meteorological Information Center of China are used to evaluate precipitation from WRF. The data are formed by merging ground observation over land and satellite retrieval over ocean (Joyce et al. 2004), with spatial resolution of  $0.25^\circ \times 0.25^\circ$ . In the merging procedure, the original Climate Precipitation Center Morphing satellite precipitation products are reprocessed and calibrated by available ground observations, which reduces the random errors and systematic biases of the satellite products (Xie and Xiong 2011). A quantitative assessment reported by Shen et al. (2014) showed that the merged data are of very good quality over mainland China. The northward migration of the EASM precipitation belt (monsoon front) is often accompanied by a strong convective system, and the corresponding precipitation is dominated by convective precipitation (Ding and Chan 2005; Chen et al. 2017). Therefore, the location of maximum precipitation is regarded as the convective center in this paper.

The ERA-Interim is used to evaluate the simulated circulation fields in this study. ERA-Interim is a very good meteorological reanalysis dataset, with many aspects improved compared to its predecessor, including the representation of the hydrological cycle, the quality of the stratospheric circulation, and the consistency in time of the reanalyzed fields (Dee et al. 2011). The ERA-Interim data can well describe atmospheric temperature, winds and humidity, including their diurnal variation in East Asia (Bao and Zhang 2013; Chen et al. 2014).

### 2.2 Model configuration in the control simulation

Advanced Research WRF version 3.8.1 (ARW v3.8.1) is used to study the impact of CVS on EASM precipitation belt. The IWC and LWC in WRF model are mainly controlled by the microphysics and cumulus convective parameterization schemes. Commonly used microphysics parameterization schemes as Lin, WSM6, Thompson, Morrison and cumulus convective parameterization schemes as Kain-Fritsch and Grell-Freitas are selected to evaluate atmospheric circulation and precipitation during the northward progress of the East Asian summer monsoon. The best performance is obtained with the configuration using the WSM6 microphysics scheme (Hong and Lim, 2006), the Xu-Randall cloud-fraction scheme (Xu and Randall

1996), the Kain-Fritsch cumulus convective parameterization scheme (Kain, 2004), the CAM radiation scheme (Collins et al. 2006), the YSU planetary boundary layer scheme (Hong et al. 2006), the revised MM5 Monin-Obukhov surface layer scheme (Jiménez et al. 2012), and the Noah land surface scheme (Chen and Dudhia 2001). The Lambert map projection is used with the standard longitude at 115°E, the simulation center at (105°E, 30°N), and the horizontal grid spacing is 30 km. There are 241 grid points in the east-west direction, 179 grid points in the north-south direction, 30 layers in the vertical, and the top pressure of the model is 50 hPa. The ERA-Interim data are used as the initial field and boundary conditions to drive WRF, and the boundary field contains 1 fixed boundary layer and 9 relaxing layers. The deep soil temperature and sea surface temperature provided by ERA-Interim are also updated every 6 h.

A strong northward-shifting EASM event occurred in June 2007. There were three distinct precipitation episodes from June 6 to June 22 (Beijing time, idem hereafter). The northward shift is an obvious feature, constituting a typical northward-shifting EASM event. The daily precipitation observed in China is reported as accumulated amount from 20:00 of the previous day to 20:00 on the nominative day. To match the precipitation timing, our study time is set from 20:00 on June 5 to 20:00 on June 22. The first 24 h of the

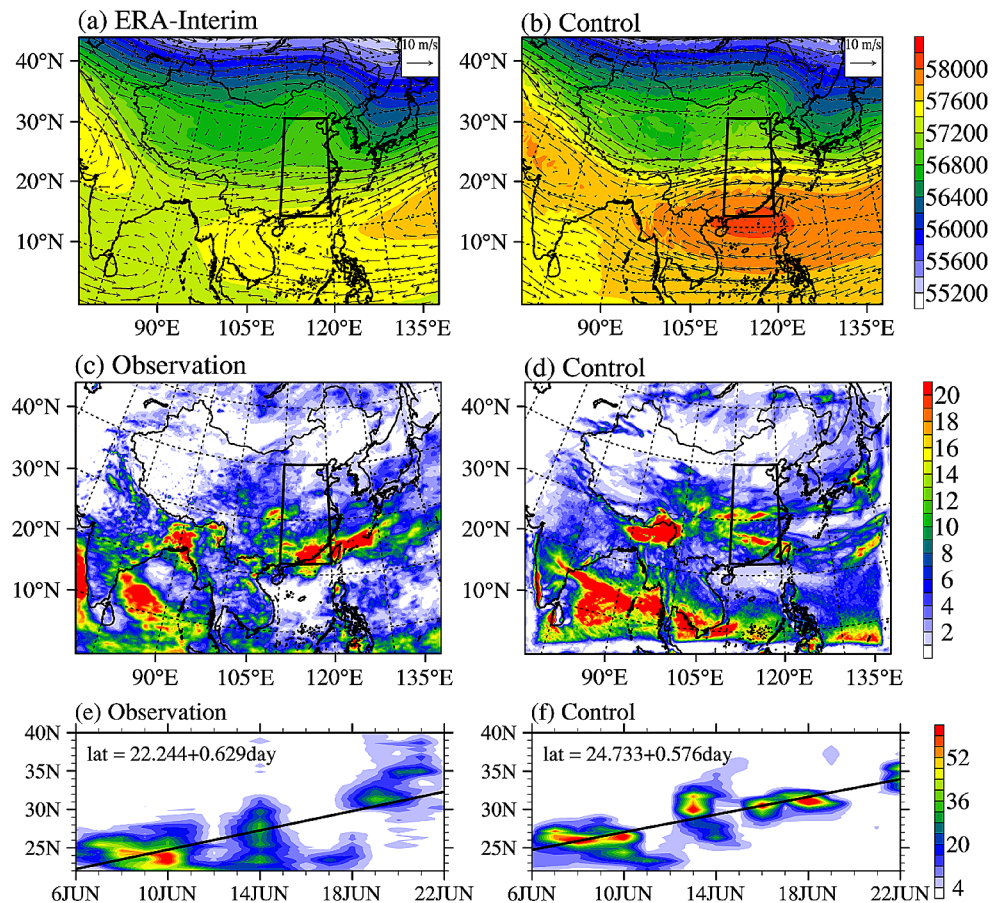
simulation are taken as spin-up time, so the model is running from 20:00 on June 4 to 20:00 on June 22. The integration time step is 120 s, and the simulation output is recorded every 3 h.

### 2.3 Evaluation of the WRF model

Large-scale atmospheric circulation is the key indicator to assess against the ERA-Interim reanalysis data and WRF simulations. Although the simulated 500 hPa geopotential height (HGT) and wind speed are slightly larger, WRF is able to reproduce the basic characteristics of the regional atmospheric circulation (Fig. 1a-b) and its northward shift (figure omitted). Simulated precipitation is larger in the tropics, but WRF well represents the spatial distribution and northward shift of the precipitation belt (Fig. 1c-f).

Hourly averaged precipitation (averaged from 110°E to 120°E) is used to determine the position of the convective center (black line in Fig. 1e). There are three precipitation episodes during our simulation. They represent a typical northward shift of the EASM front and related precipitation belt. Such simulated features are consistent with observation (Fig. 1f). A linear regression is performed in the meridional-temporal diagram of precipitation to estimate the northward-shifting speed of the EASM precipitation belt,

**Fig. 1** Averaged 500 hPa HGT (shaded, unit: gpm) and wind (vector, unit: m/s) of the (a) ERA-Interim and (b) WRF. Spatial distribution of accumulated precipitation (unit: mm/day) of the (c) observation and (d) WRF. Daily precipitation (unit: mm/day) averaged from 110°E to 120°E during June 6 to June 22 in (e) observation and (f) WRF. The black line indicates the linearly fitted precipitation center



about 0.576 degrees of latitude per day, which is also very close to the observation of 0.629 degrees of latitude per day.

## 2.4 Construction of the tilted CVS

We use IWC and LWC from CloudSat data to construct the vertical structures of cloudiness (Fig. 2), in such a way that the CVS imposed in WRF is as close as possible to actual observations (Sun et al. 2019b). Anomalous values were calculated by IWC and LWC from June 5 to 22 in 2007 minus their climatological values (from 2006 to 2010). Composite IWC anomaly does not show any tilted structure (Fig. 2a), while LWC anomaly is northward tilted (seen from upper to lower layers, Fig. 2b).

The IWC does not show any tilted structure in the composite, and its anomalies are directly averaged in the vertical to obtain the distribution function (Fig. 3a, black curve) which is axis-symmetric around the convective center (Fig. 3a, red curve). For the sake of applicability, the distribution is further fitted with a quartic function (Fig. 3a, blue curve), and expressed as:

$$y = 47.761 + 8.126x^2 - 0.861x^4 \quad (1)$$

where  $y$  is the value of IWC and  $x$  is the distance from the convective center, expressed in degree of latitude. Finally, a new vertical structure of the IWC is constructed as a vertical cylinder (Fig. 3c). Similarly, we also use a quartic function to mimic its distribution around the convective center for LWC, as displayed in Fig. 3b, and expressed as:

$$y = 26.212 - 3.935x^2 + 0.019x^4 \quad (2)$$

However, LWC has a tilted vertical structure (a tilted cylinder, Fig. 3d). Its calculation is strongly inspired from observations.

## 2.5 Experimental design

The control simulation (CTRL) is the basic simulation performed with WRF after a careful tuning of parameterizations and parameters. It mainly serves as an assessment of WRF's performance. It also served to determine the geographical positions of convection centers (as shown in Fig. 1e-f) which are useful for the prescription of CVS in the sensitivity experiments. The comparison of CTRL and the subsequent sensitivity experiments allows us to appreciate the primary effect of introducing CVS in the model.

The sensitivity experiment protocol consists of three further simulations with artificially-modified IWC and LWC in WRF. The IWC and LWC are model variables used to calculate the impact of cloudiness on radiative transfer in WRF and to describe the cloud microphysics. To implement the above-described CVS into the model, we overwrite the model's variables QCLOUD and QICE with the reconstructed LWC and IWC structures (Fig. 3c-d) from CloudSat observations, respectively. We use the convective center to locate our imposed CVS. When LWC and IWC is perturbed, other geophysical variables are also affected and they make adjustment to follow the new configuration. The operation is performed at each time step involving clouds, and in a dynamic way following the linear track deduced from the convective centers in the CTRL (black line in Fig. 1f). We also take into account the northward displacement of the synoptic system during our investigation period. In the meridional direction, there was a general northward displacement during the time of our interest, but high-frequency irregular north-south movements were still observed. For our purpose, we just ignore these movements by using a linear function to approximate the change of position in latitude. Sensitivity experiments are as follows:

(1) Test CWC-V. The tilting angle of LWC is zero (no tilting configuration).

(2) Test CWC-N. The profile of IWC/LWC is northward tilted (roughly from the middle troposphere to the surface).

**Fig. 2** Composite (a) ice water content (IWC) and (b) liquid water content (LWC) anomalies ( $10^{-6}$  kg/kg) from CloudSat data following the convective center during the northward-shift of the EASM precipitation belt from 5 to 22 June 2007. The X-axis is the relative distance to the convective center in degree of latitude, negative values indicate south to the convective center, and positive values north to the convective center

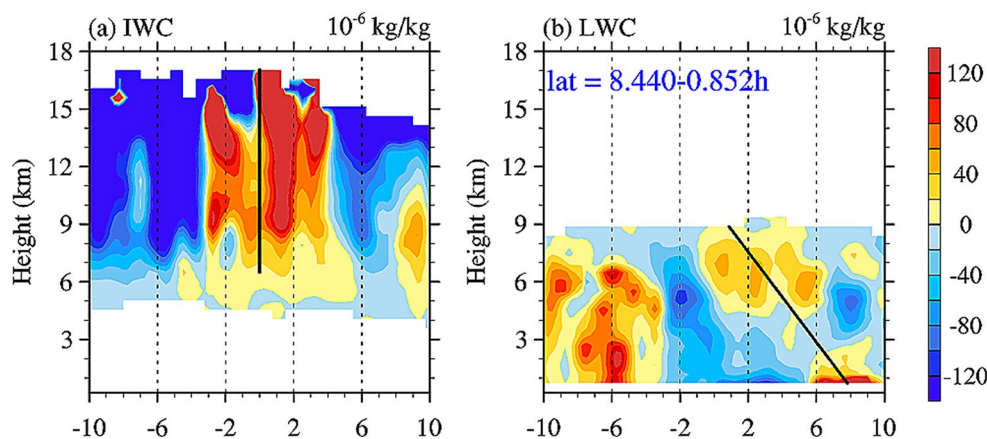


**Fig. 3** Distribution function of the (a) IWC and (b) LWC anomalies (black: vertical average; red: averaged on both sides of the convective center; blue: quartic fitting curve). The constructed vertical structure of the (c) IWC and (d) LWC anomalies (unit:  $\times 10^{-6}$  kg/kg). The values of the X-axis are the relative distance to the convective center in degree of latitude, negative values indicate southern distances to the convective center, and positive values indicate northern distances to the convective center

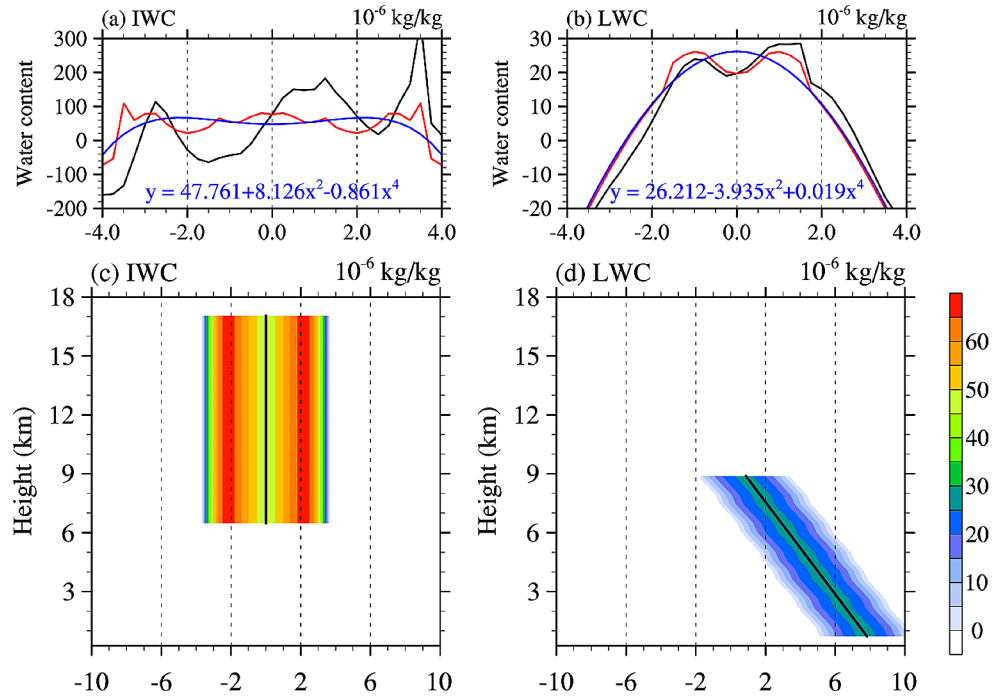
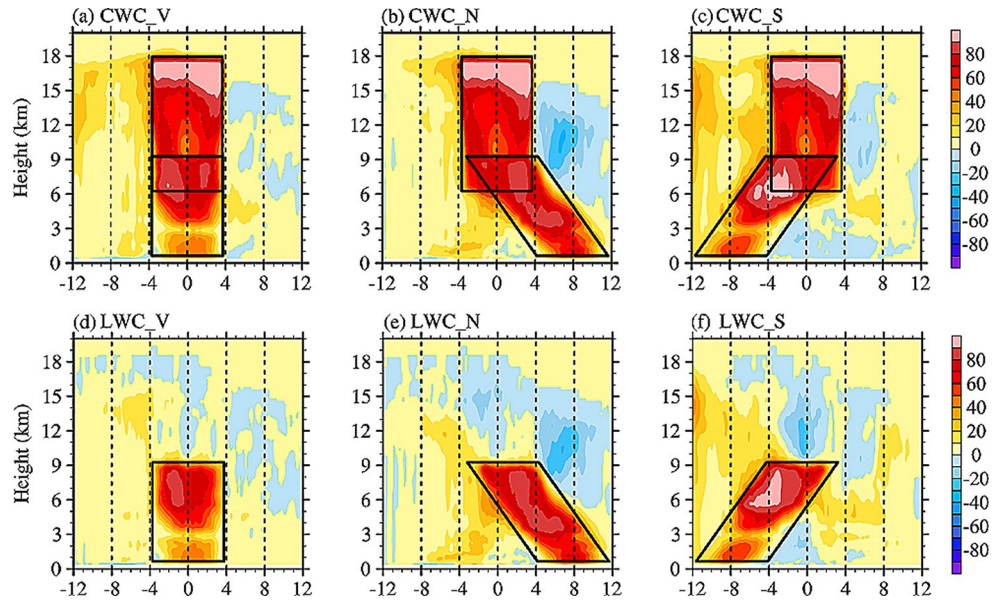


**Fig. 4** Compositd vertical cloud amount (unit: %) at 115°E based on daily convective centers from June 6 to 22. (a-c) imposed both IWC and LWC, while (d-f) only imposed LWC. The black quadrangles show vertical structure of imposed IWC and LWC in WRF. The X-axis is the same as in Fig. 2



(3) Test CWC-S. The same as test CWC-N, but the tilting angle of LWC is inversed (opposite to what observed).

To isolate the only effect of tilting LWC with IWC unchanged, we also design a second set of sensitivity simulations, with only LWC profiles imposed in the model. They are referred to as LWC-V, LWC-N, LWC-S, respectively.

Figure 4 shows the vertical profile of the composite cloud amount at 115°E from June 6 to 22 in CWC and LWC experiments. Black quadrangles mark the vertical structure of IWC and LWC imposed in the model. As shown in Fig. 4, cloud amount increased significantly in the regions where CWC imposed in the experiments. There is no tilted vertical

structure in CWC-V and LWC-V experiments, while the CVS tilts northward (southward) from upper to lower in CWC-N and LWC-N (CWC-S and LWC-S) experiments. Compared with the CTRL, cloud amount extends from the upper troposphere to the near surface in the CWC experiments (Fig. 4a-c), while remains in the lower and middle troposphere in the LWC experiments (Fig. 4d-f).

### 3 Impact of the tilted CVS

Compared with CTRL (Fig. 1f), the sensitivity experiments show significantly increased precipitation after imposing CWC (Fig. 5a-f). When the CVS without tilt is imposed, only the values of precipitation are increased, but the precipitation belt has little changes (Fig. 5a). The precipitation belt significantly shifts northward when the CVS is northward tilted (Fig. 5b). In contrast, the precipitation belt shifts southward substantially when imposing the southward tilted CVS (Fig. 5c). These results suggest that changing the CVS can affect the direction and speed of the EASM movement. The variation of the precipitation belt by only changing LWC (Fig. 5d-f) is very similar to that by changing both LWC and IWC (Fig. 5a-c). Changes in the precipitation belt are mainly caused by changes in the LWC. Therefore, only the impact of vertical structure of the LWC on the EASM precipitation belt is analyzed in the following.

To further highlight the impact of CVS on EASM precipitation, the differences in 500 hPa HGT and wind fields between the LWC experiments and CTRL are shown in Fig. 6. The CVS has little effect on the EASM precipitation belt at the beginning. Negative anomaly of 500 hPa HGT in the LWC-V experiment is nearly located in the convective center, so the location of the precipitation belt in LWC-V experiment has little change. Imposing LWC only causes the increase of precipitation amount. With the change in vertical structure of the LWC, the CVS has increasingly more influence on the EASM precipitation belt and affects more surrounding areas. The HGT on the northern side of the convective center decreases after imposing the northward tilted CVS and is accompanied by cyclonic wind field differences, which is conducive to the northward shift of the precipitation belt. However, when the southward tilted CVS is imposed, HGT on the southern (northern) side of

the convective center decreases (increases), which is not conducive to the northward shift of the precipitation belt. Therefore, the LWC-S experiment has a slower northward shift of the precipitation belt.

To clearly show the change in vertical atmospheric circulation, hourly HGT difference between the sensitivity experiment and CTRL on the 115°E vertical section (Fig. 7). As previously practiced, the diagrams were composited ones during June 6 to June 22 following the moving convective center (Fig. 1f). There is no significant HGT difference between the north and south sides of the convective center when LWC without tilt is imposed (Fig. 7a), so there is no significant change in the EASM precipitation belt. Negative HGT anomaly is located at approximately 6 degrees north of the convective center, with a drop up to 3 gpm (Fig. 7b), which increases the meridional wind speed and promotes the northward shift of the precipitation belt. Conversely, when the southward tilted LWC is imposed, negative HGT anomaly is located in the middle and lower troposphere south of the convective center, while opposite on the northern side (Fig. 7c). The variation in HGT decreases the meridional wind speed, which is not favorable to the northward shift of the EASM precipitation belt.

### 4 Explanation on the role of tilted CVS

Clouds in WRF are regrouped into three types: stratiform clouds, deep convective clouds and shallow convective clouds. Figure 8 shows the composite difference of LWC in stratiform clouds, deep convective clouds and shallow convective clouds on the 115°E vertical section. Stratiform clouds increase significantly after imposing LWC in the model, and its amount increases more than 40% in the region where LWC is imposed (Fig. 8a-c). Deep convective

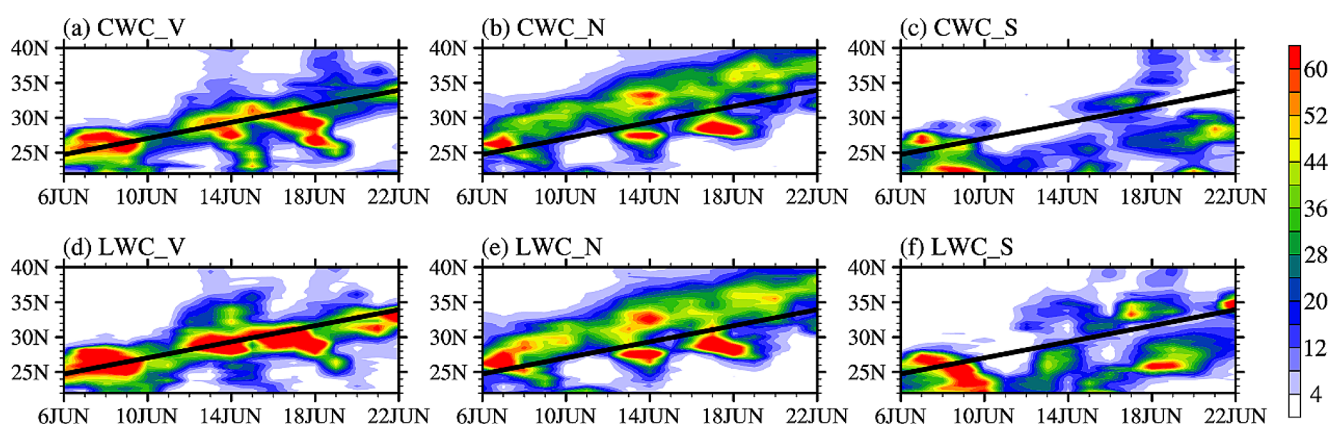


**Fig. 5** Daily precipitation averaged from 110°E to 120°E during June 6 to June 22 (unit: mm/day). (a-c) Imposing the IWC and LWC, (d-f) imposing only the LWC, (a, d) imposing the CVS without tilt, (b, e) imposing the northward tilted CVS from the upper to the lower atmo-

sphere, and (c, f) imposing the southward tilted CVS from the upper to the lower atmosphere. The black solid line is the fitted precipitation center

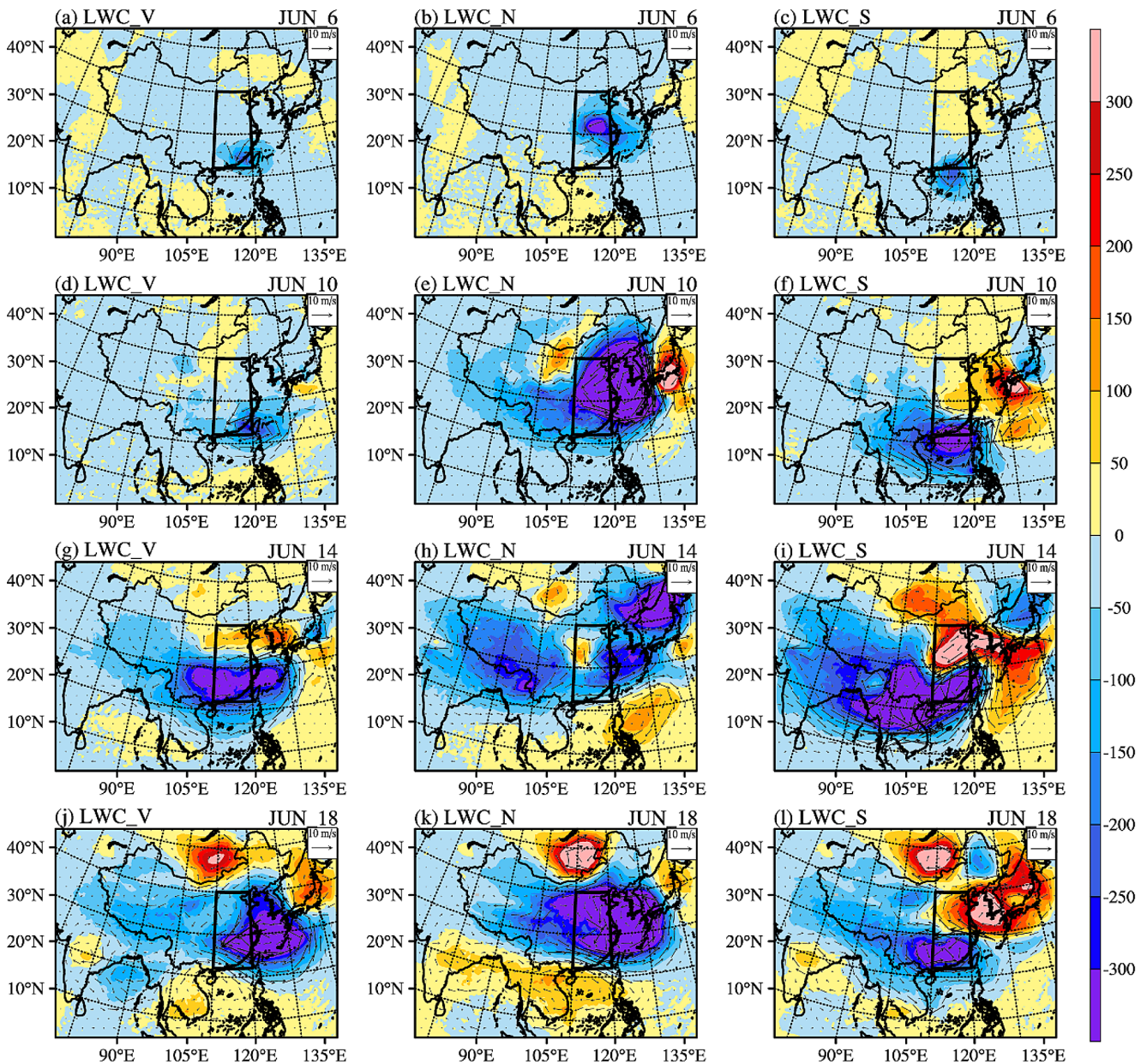
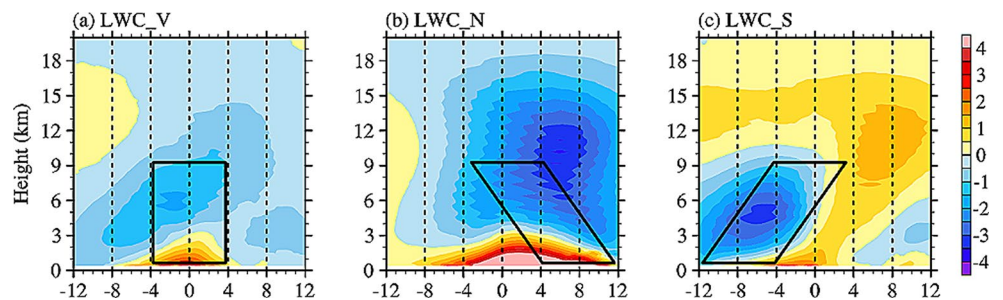


**Fig. 6** Differences in the 500 hPa HGT (shaded, unit: gpm) and the wind field (vector, unit: m/s) between the LWC experiments and the CTRL on (a-c) June 6, (d-f) June 10, (g-i) June 14 and (j-l) June 18. Tests (a, d, g, j) LWC-V, (b, e, h, k) LWC-N and (c, f, i, l) LWC-S

**Fig. 7** Differences in composited HGT on the 115°E vertical section between the LWC experiments and CTRL (unit: gpm) during June 6–22. Tests (a) LWC-V, (b) LWC-N and (c) LWC-S. The X-axis and black quadrilateral are same as Fig. 4d-f



cloud amount near the convective center decreases after imposing LWC (Fig. 8d-f), and so is the convective precipitation. Area with increased precipitation is consistent with the area of increased stratiform clouds (Fig. 8g-i).

In the LWC-V experiments, shallow convective cloud amount varies slightly and basically remains unchanged (Fig. 8g). However, shallow convective clouds increase significantly at about 8 degrees north (south) of the convective center in the LWC-N (LWC-S) experiment (Fig. 8g-i). That is, shallow convection is significantly enhanced when LWC is imposed in lower atmosphere, and the maximum increase is up to 10%. Most notably, the shallow convective clouds, which were generally less than 6% in CTRL, correspond to a large increase and appear in the direction that guides the EASM movement. Thus, the shallow convective clouds may have an important impact on the EASM precipitation belt.

In the following, the LWC-N experiment is used as an example to explain the impact of the CVS on the EASM precipitation belt. With the addition of LWC, an increase in cloud water leads to an increase of evaporation in clouds (Fig. 9a), and an increase of atmospheric water vapor. Evaporation of cloud water is endothermic, thereby reducing

atmospheric temperature (Fig. 9c). Low-temperature and high-humidity air is located on the north side of the convective center, which is more conducive to precipitation on the north side of the convective center and promotes the northward shift of the precipitation belt. Water vapor decreases and temperature increases on the north side of the convective center in the sensitivity experiments (Fig. 9b and d), indicating weakened deep convective activity. With increased shallow convective clouds, condensation heating of shallow convection in the lower troposphere increases significantly, water vapor and energy transport from lower troposphere to free atmosphere increase accordingly. Both of these factors would cause the decrease of HGT north of the convective center, thereby promoting the northward shift of the EASM precipitation belt.

## 5 Conclusions

Impact of the CVS on the EASM precipitation belt was explored in this paper. When LWC is imposed without tilt, there is no significant HGT difference and no obvious change in the precipitation belt. When the northward

**Fig. 8** Same as Fig. 7 but for (a-c) stratiform cloud amount (unit: %), (d-f) deep convective cloud amount (unit: %), (g-i) shallow convective cloud amount (upper part, unit: %) and precipitation (lower part, unit: mm/day)

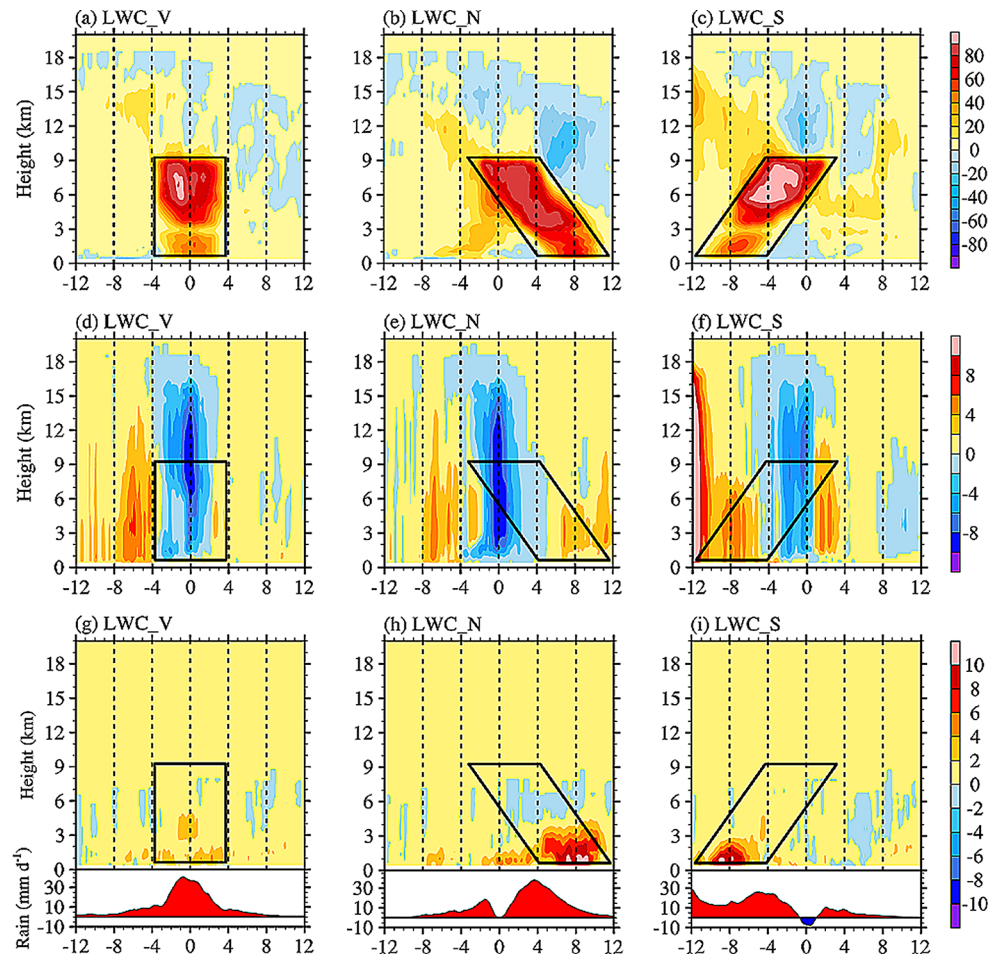
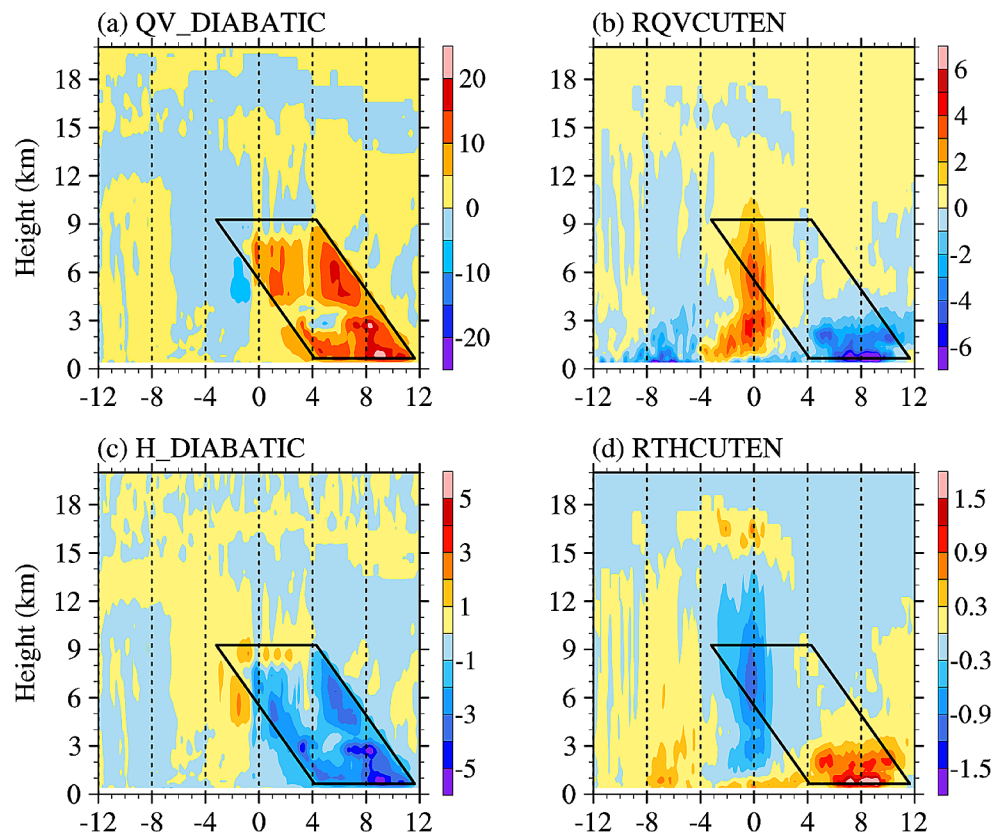




**Fig. 9** Same as Fig. 7a but for (a) water vapor tendency due to microphysical processes (unit:  $10^{-8}$  kg/kg  $s^{-1}$ ), (b) water vapor tendency due to cumulus convection (unit:  $10^{-8}$  kg/kg  $s^{-1}$ ), (c) temperature tendency due to microphysical processes (unit:  $10^{-4}$  K  $s^{-1}$ ) and (d) temperature tendency due to cumulus convection (unit:  $10^{-4}$  K  $s^{-1}$ )



tilted LWC is imposed, negative HGT anomaly is located at approximately 6 degrees north of the convective center, up to 3 gpm. The HGT anomaly increases the meridional wind speed and promotes the northward shift of the precipitation belt. However, when the southward tilted LWC is imposed, HGT decreases in the middle and lower troposphere south of the convective center and increases on the northern side. The HGT anomaly can reduce the meridional wind speed, which is not conducive to the northward shift of the precipitation belt.

In the case that LWC is imposed to the model, evaporation of cloud water leads to an increase in atmospheric humidity and a decrease in atmospheric temperature. The increase in stratiform clouds is more than 40%, accompanied with more stratiform precipitation. In the LWC-N experiment, air with low temperature and high humidity is located on the north side of the convective center, leading to northward shift of the precipitation belt. In contrast, deep convection is weakened, and convective precipitation is reduced significantly. Most notably, with the enhancement of shallow convection, condensation heating in the lower troposphere is significantly increased. Therefore, more water vapor and energy are transported from the boundary layer to the free atmosphere. The geopotential height in north of the convective center is reduced, thereby promoting the northward shift of the precipitation belt.

An artificially imposed northward tilted CVS partly influences the water vapor balance in WRF model, but we believe the conclusions are credible. The injected perturbation is small enough to be below the model's tolerance. The model takes into account the imposed LWC, environmental fields adjust with the experimental designed cloud structure. Actually, there is no unstable configurations in our sensitivity experiments. In our case, two physical processes are involved, one is the radiative effect in relation to radiative transfer in the atmosphere, another is the thermodynamics in relation to changes of water phases. Our current design is not able to make the right distinction between them. From the obtained results, it seems that the thermodynamic effect is the dominant one. We should perform further sensitivity experiments to deepen our investigation in the future.

**Author contributions** L.Y. Y. conceptualized this study and led the writing. S. G. R. analyzed the data and wrote the original draft. Z. Z. W., L. Z. X. and Z. C. interpreted the results and revised the text. All authors contributed to this work and approved the final manuscript before submission.

**Funding** This research was supported by the National Natural Science Foundation of China (Grant No.42075077, U2242201), and Hunan Provincial Natural Science Foundation of China (Grant No. 2021JC0009).

**Data availability** The CloudSat data used in this study were obtained from the CloudSat website (<http://www.cloudsat.cira.colostate.edu>).

The merged daily precipitation data used in this study were obtained from the National Meteorological Information Center website (<http://data.cma.cn>). The ERA-Interim data used in this study were obtained from the ECMWF website (<https://www.ecmwf.int>).

## Declarations

**Consent for publication** All authors have read the manuscript and agreed to publish.

**Conflict of interest** The authors declare no competing interests.

**Open Access** This article is licensed under a Creative Commons Attribution 4.0 International License, which permits use, sharing, adaptation, distribution and reproduction in any medium or format, as long as you give appropriate credit to the original author(s) and the source, provide a link to the Creative Commons licence, and indicate if changes were made. The images or other third party material in this article are included in the article's Creative Commons licence, unless indicated otherwise in a credit line to the material. If material is not included in the article's Creative Commons licence and your intended use is not permitted by statutory regulation or exceeds the permitted use, you will need to obtain permission directly from the copyright holder. To view a copy of this licence, visit <http://creativecommons.org/licenses/by/4.0/>.

## References

- Austin RT, Heymsfield AJ, Stephens GL (2009) Retrieval of ice cloud microphysical parameters using the CloudSat millimeter-wave radar and temperature. *J Geophys Res* 114:D00A23. <https://doi.org/10.1029/2008JD010049>
- Bao X, Zhang F (2013) Evaluation of NCEP–CFSR, NCEP–NCAR, ERA-Interim, and ERA-40 reanalysis datasets against Independent Sounding observations over the Tibetan Plateau. *J Clim* 26:206–214. <https://doi.org/10.1175/JCLI-D-12-00056.1>
- Cao G, Zhang GJ (2017) Role of Vertical structure of Convective Heating in MJO Simulation in NCAR CAM5.3. *J Clim* 30:7423–7439. <https://doi.org/10.1175/JCLI-D-16-0913.1>
- Cesana G, Chepfer H (2012) How well do climate models simulate cloud vertical structure? A comparison between CALIPSO–GOCCP satellite observations and CMIP5 models. *Geophys Res Lett* 39:2012GL053153. <https://doi.org/10.1029/2012GL053153>
- Chen F, Dudhia J (2001) Coupling an Advanced Land surface–hydrology model with the Penn State–NCAR MM5 modeling system. Part I: model implementation and sensitivity. *Mon Weather Rev* 129:569–585. [https://doi.org/10.1175/1520-0493\(2001\)129<0569:CAALSH>2.0.CO;2](https://doi.org/10.1175/1520-0493(2001)129<0569:CAALSH>2.0.CO;2)
- Chen G, Iwasaki T, Qin H, Sha W (2014) Evaluation of the warm-season diurnal variability over East Asia in recent reanalyses JRA-55, ERA-Interim, NCEP CFSR, and NASA MERRA. *J Clim* 27:5517–5537. <https://doi.org/10.1175/JCLI-D-14-00005.1>
- Chen T-C, Tsay J-D, Matsumoto J (2017) Interannual variation of the Summer Rainfall Center in the South China Sea. *J Clim* 30:7909–7931. <https://doi.org/10.1175/JCLI-D-16-0889.1>
- Collins WD, Rasch PJ, Boville BA et al (2006) The Formulation and Atmospheric Simulation of the Community Atmosphere Model Version 3 (CAM3). *J Clim* 19:2144–2161. <https://doi.org/10.1175/JCLI3760.1>
- Dee DP, Uppala SM, Simmons AJ et al (2011) The ERA-Interim reanalysis: configuration and performance of the data assimilation system. *Q J R Meteorol Soc* 137:553–597. <https://doi.org/10.1002/qj.828>
- Ding Y, Chan JCL (2005) The east Asian summer monsoon: an overview. *Meteorol Atmospheric Phys* 89:117–142. <https://doi.org/10.1007/s00703-005-0125-z>
- Hill PG, Allan RP, Chiu JC et al (2018) Quantifying the contribution of different cloud types to the Radiation Budget in Southern West Africa. *J Clim* 31:5273–5291. <https://doi.org/10.1175/JCLI-D-17-0586.1>
- Hong S-Y, Noh Y, Dudhia J (2006) A New Vertical Diffusion Package with an Explicit treatment of entrainment processes. *Mon Weather Rev* 134:2318–2341. <https://doi.org/10.1175/MWR3199.1>
- Hong Y, Liu G, Li J-LF (2016) Assessing the Radiative effects of Global Ice clouds based on CloudSat and CALIPSO measurements. *J Clim* 29:7651–7674. <https://doi.org/10.1175/JCLI-D-15-0799.1>
- Jakob C, Klein SA (1999) The role of vertically varying cloud fraction in the parametrization of microphysical processes in the ECMWF model. *Q J R Meteorol Soc* 125:941–965. <https://doi.org/10.1002/qj.49712555510>
- Jiang JH, Su H, Zhai C et al (2012) Evaluation of cloud and water vapor simulations in CMIP5 climate models using NASA A-Train satellite observations: EVALUATION OF IPCC AR5 MODEL SIMULATIONS. *J Geophys Res Atmos* 117. <https://doi.org/10.1029/2011JD017237>
- Jiménez PA, Dudhia J, González-Rouco JF et al (2012) A revised Scheme for the WRF Surface Layer Formulation. *Mon Weather Rev* 140:898–918. <https://doi.org/10.1175/MWR-D-11-00056.1>
- Joyce RJ, Janowiak JE, Arkin PA, Xie P (2004) CMORPH: a method that produces global precipitation estimates from Passive Microwave and Infrared data at high spatial and temporal resolution. *J Hydrometeorol* 5:487–503. [https://doi.org/10.1175/1525-7541\(2004\)005<0487:CAMTPG>2.0.CO;2](https://doi.org/10.1175/1525-7541(2004)005<0487:CAMTPG>2.0.CO;2)
- Klein SA, Zhang Y, Zelinka MD et al (2013) Are climate model simulations of clouds improving? An evaluation using the ISCCP simulator: EVALUATING CLOUDS IN CLIMATE MODELS. *J Geophys Res Atmos* 118:1329–1342. <https://doi.org/10.1002/jgrd.50141>
- Kusunoki S, Arakawa O (2015) Are CMIP5 models better than CMIP3 models in simulating precipitation over East Asia? *J Clim* 28:5601–5621. <https://doi.org/10.1175/JCLI-D-14-00585.1>
- Li Y, Zhang M (2017) The role of shallow convection over the Tibetan Plateau. *J Clim* 30:5791–5803. <https://doi.org/10.1175/JCLI-D-16-0599.1>
- Li S, Li Y, Sun G, Lu Z (2018) Macro- and microphysical characteristics of Precipitating and Non-precipitating Stratocumulus clouds over Eastern China. *Atmosphere* 9:237. <https://doi.org/10.3390/atmos9070237>
- Luo Y, Zhang R, Qian W et al (2011) Intercomparison of Deep Convection over the Tibetan Plateau–Asian Monsoon Region and Subtropical North America in Boreal Summer using CloudSat/CALIPSO Data. *J Clim* 24:2164–2177. <https://doi.org/10.1175/2010JCLI4032.1>
- McFarlane SA, Mather JH, Ackerman TP, Liu Z (2008) Effect of clouds on the calculated vertical distribution of shortwave absorption in the tropics. *J Geophys Res* 113:D18203. <https://doi.org/10.1029/2008JD009791>
- Shen Y, Zhao P, Pan Y, Yu J (2014) A high spatiotemporal gauge-satellite merged precipitation analysis over China. *J Geophys Res Atmos* 119:3063–3075. <https://doi.org/10.1002/2013JD020686>
- Stephens G, Winker D, Pelon J et al (2018) CloudSat and CALIPSO within the A-Train: ten years of actively observing the Earth System. *Bull Am Meteorol Soc* 99:569–581. <https://doi.org/10.1175/BAMS-D-16-0324.1>
- Sun G, Li Y, Liu L (2019a) Why is there a tilted cloud vertical structure associated with the northward advance of the east Asian summer monsoon. *Atmospheric Sci Lett* 20:e903. <https://doi.org/10.1002/asl.903>

- Sun G, Li Y, Lu J (2019b) Cloud vertical structures associated with northward advance of the east Asian summer monsoon. *Atmospheric Res* 215:317–325. <https://doi.org/10.1016/j.atmosres.2018.09.013>
- Turner DD, Shupe MD, Zwink AB (2018) Characteristic Atmospheric Radiative Heating Rate profiles in Arctic clouds as observed at Barrow, Alaska. *J Appl Meteorol Climatol* 57:953–968. <https://doi.org/10.1175/JAMC-D-17-0252.1>
- Wang J, Rossow WB (1998) Effects of Cloud Vertical structure on Atmospheric circulation in the GISS GCM. *J Clim* 11:3010–3029. [https://doi.org/10.1175/1520-0442\(1998\)011<3010:EOCVSO>2.0.CO;2](https://doi.org/10.1175/1520-0442(1998)011<3010:EOCVSO>2.0.CO;2)
- Wang J, Rossow WB, Zhang Y (2000) Cloud Vertical structure and its variations from a 20-Yr global rawinsonde dataset. *J Clim* 13:3041–3056. [https://doi.org/10.1175/1520-0442\(2000\)013<3041:CVSAIV>2.0.CO;2](https://doi.org/10.1175/1520-0442(2000)013<3041:CVSAIV>2.0.CO;2)
- Weare BC (2000) Insights into the importance of cloud vertical structure in climate. *Geophys Res Lett* 27:907–910. <https://doi.org/10.1029/1999GL011214>
- Xie P, Xiong A-Y (2011) A conceptual model for constructing high-resolution gauge-satellite merged precipitation analyses: GAUGE-SATELLITE MERGED PRECIP ANALYSIS. *J Geophys Res Atmos* 116. <https://doi.org/10.1029/2011JD016118>
- Xu K-M, Randall DA (1996) A Semiempirical cloudiness parameterization for Use in Climate models. *J Atmospheric Sci* 53:3084–3102. [https://doi.org/10.1175/1520-0469\(1996\)053<3084:ASCPFU>2.0.CO;2](https://doi.org/10.1175/1520-0469(1996)053<3084:ASCPFU>2.0.CO;2)
- Yan Y-F, Wang X-C, Liu Y-M (2018) Cloud vertical structures associated with precipitation magnitudes over the Tibetan Plateau and its neighboring regions. *Atmospheric Ocean Sci Lett* 11:44–53. <https://doi.org/10.1080/16742834.2018.1395680>
- Yuan J, Houze RA, Heymsfield AJ (2011) Vertical structures of Anvil clouds of Tropical Mesoscale Convective systems observed by CloudSat. *J Atmospheric Sci* 68:1653–1674. <https://doi.org/10.1175/2011JAS3687.1>
- Zelinka MD, Klein SA, Taylor KE et al (2013) Contributions of different cloud types to Feedbacks and Rapid adjustments in CMIP5\*. *J Clim* 26:5007–5027. <https://doi.org/10.1175/JCLI-D-12-00555.1>
- Zhang Y, Li J (2013) Shortwave cloud radiative forcing on major stratus cloud regions in AMIP-type simulations of CMIP3 and CMIP5 models. *Adv Atmospheric Sci* 30:884–907. <https://doi.org/10.1007/s00376-013-2153-9>
- Zhang Z, Li Y (2020) Spring Planetary Boundary Layer structure and corresponding cloud characteristics under different prevailing wind directions over the Kuroshio Sea Surface Temperature Front in the East China Sea. *J Geophys Res Atmos* 125. <https://doi.org/10.1029/2020JD034006>
- Zhang Z, Li Y, Song W (2020) Stratocumulus in the cold and warm sides of the Spring Kuroshio Sea Surface Temperature Front in the East China Sea. *J Geophys Res Atmos* 125. <https://doi.org/10.1029/2019JD032176>

**Publisher's Note** Springer Nature remains neutral with regard to jurisdictional claims in published maps and institutional affiliations.